Supplementary material for:

Chromatic aberrations correction of attosecond high-order harmonic beams by flat-top spatial shaping of the fundamental beam

K. Veyrinas[1*], M. Plach[2*], J. Peschel[2], M. Hoflund[2], F. Catoire[1], C. Valentin[1], P. Smorenburg[3], H. Dacasa[2], S. Maclot[2#], C. Guo[2], H. Wikmark[2], A. Zaïr[4], V. Strelkov[5,6], C. Picot[7], C. Arnold[2], P. Eng-Johnsson[2], A. L'Huillier[2], E. Mével[1] and E. Constant[7]

[1]Centre Lasers Intenses et Applications (CELIA), Université de Bordeaux-CNRS-CEA, 33405 Talence Cedex, France
[2]Department of Physics, Lund University, SE-221 00 Lund, Sweden
[3]ASML Research, ASML Netherlands B.V., 5504 DR Veldhoven, The Netherlands
[4]King's College London, Department of Physics, Attosecond Physics Laboratory, Strand WC2R 2LS London, United Kingdom
[5]Prokhorov General Physics Institute of the Russian Academy of Sciences, 38, Vavilova Street, Moscow 119991, Russia.
[6]Moscow Institute of Physics and Technology (State University), 141700 Dolgoprudny, Moscow Region, Russia
[7]Université Claude Bernard Lyon 1, CNRS, Institut Lumière Matière (iLM), F-69622, Villeurbanne, France

* These authors contributed equally to this work.
[#] Present address: Institut Lumière Matière (iLM), Université Claude Bernard Lyon 1, CNRS, F-69622, Villeurbanne, France

E-mail: eric.constant@univ-lyon1.fr, marius.plach@fysik.lth.se

The spatial profile of the fundamental IR beam was estimated at the focus position by measuring the profile of a small fraction of the beam. Fig. S1 shows the image of the focused truncated Gaussian beam and of the spatially shaped flat-top beam.

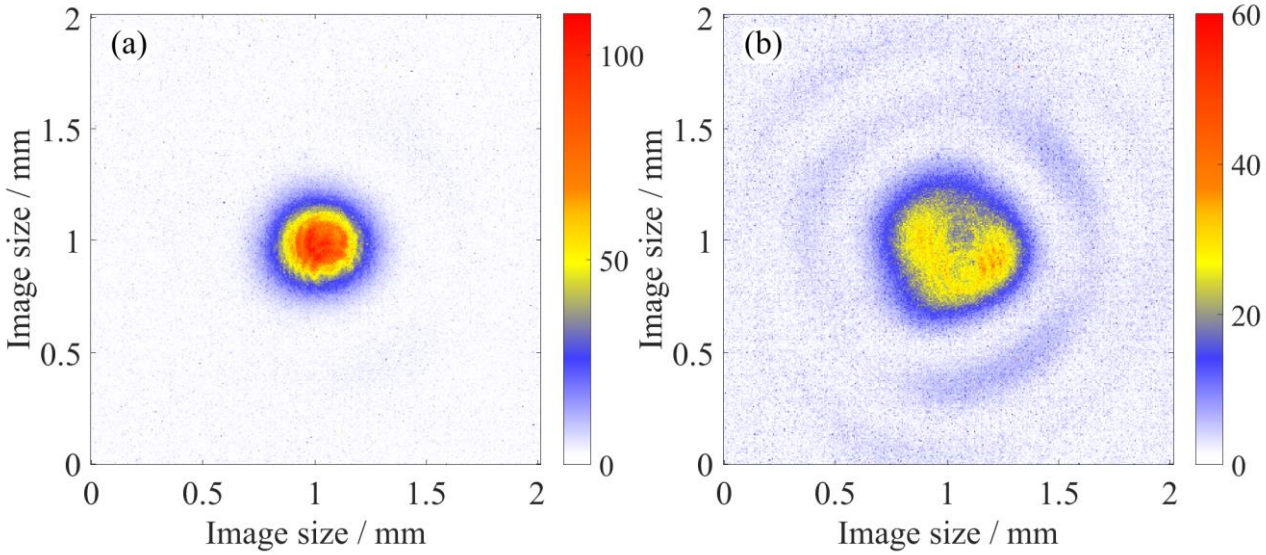

Fig. S1: Infrared spatial profile at focus (a) without the spatial shaping (incoming Gaussian beam clipped with an iris of diameter Φ_{iris} = 20 mm) and (b) with the flat-top spatial shaping (phase plate used with an iris of diameter Φ_{iris} = 27.5 mm).

The spatial profile and wavefront of the shaped beam was simulated (Fig. S2) from z = - 20 cm to z = + 20 cm (here z = 0 refers to the position of the IR focus obtained without shaping). It shows flat-top intensity profile near z = 0 and an inversion of curvature in this plane showing that the flat-top profile is achieved with this approach with a flat wavefront of the fundamental.

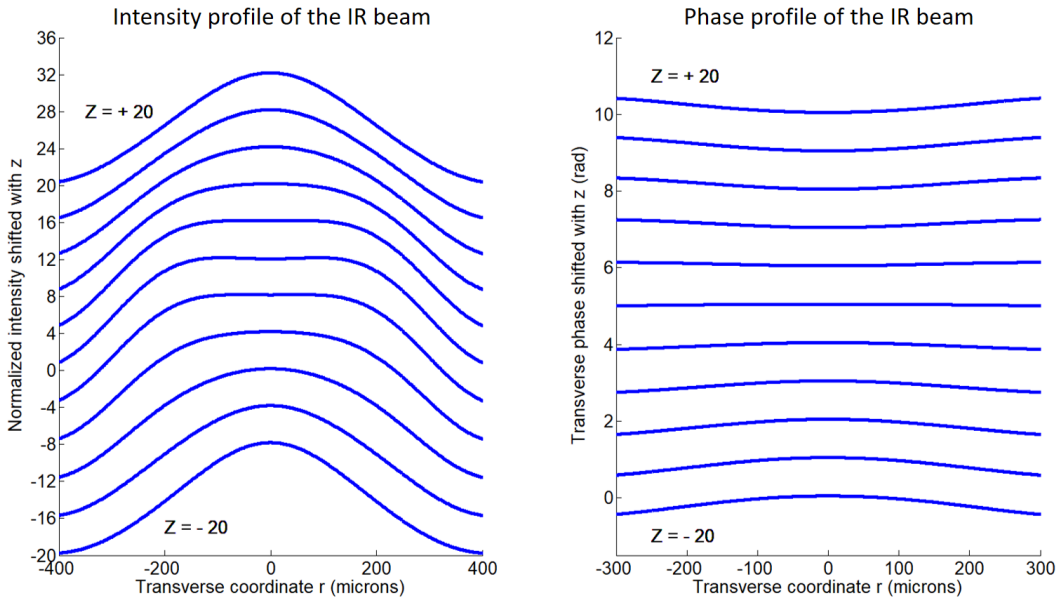

Fig. S2: Simulated spatial profiles and phase front of the flat-top IR beam shifted as a function of z (z = -20 cm to + 20 cm with 4 cm steps). Simulations performed with W = 27 mm, ϕ_{plate} = 20 mm, ϕ_{iris} = 25 mm, $\delta\varphi = \pi$. A flat-top beam shape is achieved near z = 0 and the wavefront curvature changes sign around z = 0 (here z = 0 refers to the position of the IR focus obtained without shaping). *With these parameters, the IR wavefront is flat near the flat-top position.*

The XUV spatial profiles are also directly measured with an XUV camera (Fig. S3) in which case, all harmonics transmitted by the Al filter are detected simultaneously. These images, obtained in the far field, show that the XUV beams are smaller when generated with the flat-top fundamental beam than when generated with the truncated Gaussian beam.

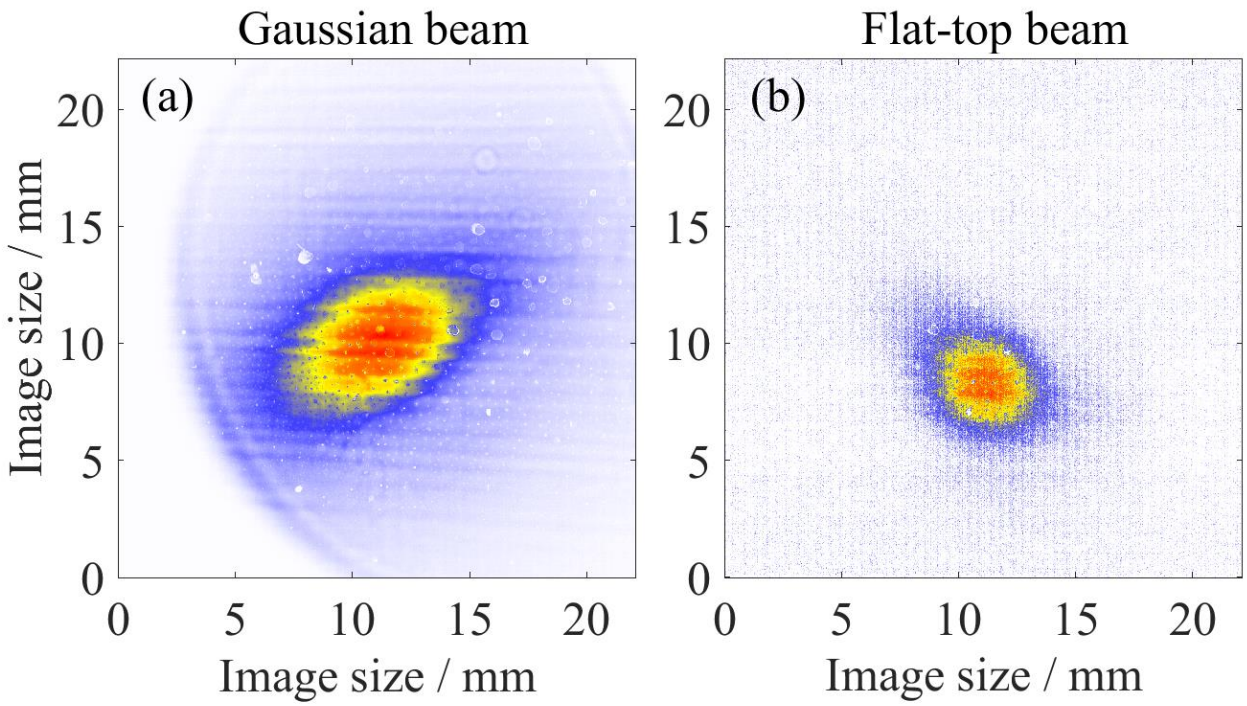

Fig. S3: Footprint of the XUV beam detected with an Andor back illuminated CCD camera. (a) Harmonics generated with a Gaussian beam, (b) Harmonics generated with a flat-top beam.

The measurements of the radii of curvature are also performed after varying parameters that are crucial in HHG such as iris diameter and pulse energy. The trends discussed in the paper are robust and reproduced under many different conditions both with the gas jet (Fig. S4(a)) and with the gas cell (Fig. S4(b)).

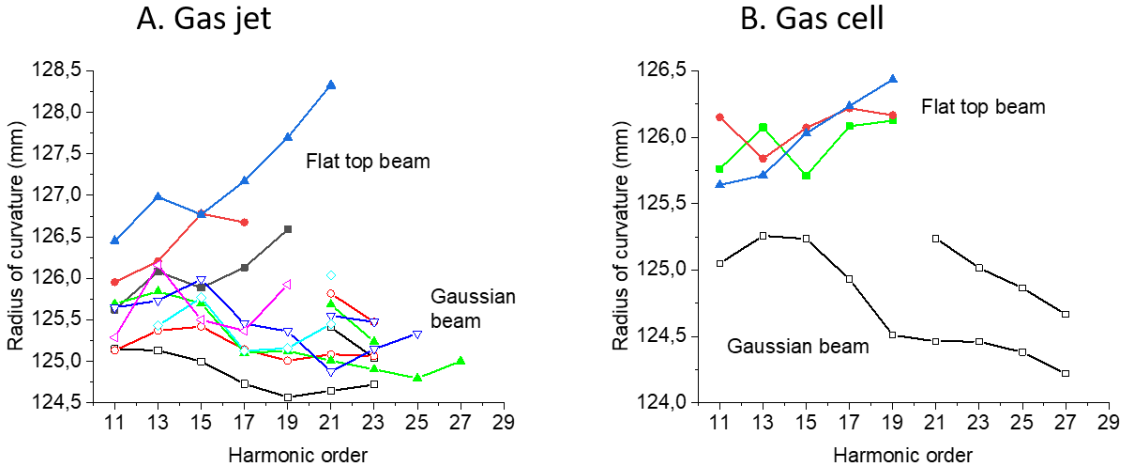

Fig. S4: Evolution of the wavefront radius of curvature with the harmonic order for harmonics generated with Gaussian beams (open symbols) and with flat-top shaped beams (full symbols) for several experimental runs where the pulse energy and iris diameter are varied. The harmonics are generated in a gas jet (a) or a 1 cm long gas cell (b).

Analog to Fig. 4 where the radius of curvature and the beam FWHM are shown under the use of a gas jet, figure S5 underlines that the trend is the same for measurements obtained with a 1 cm gas cell.

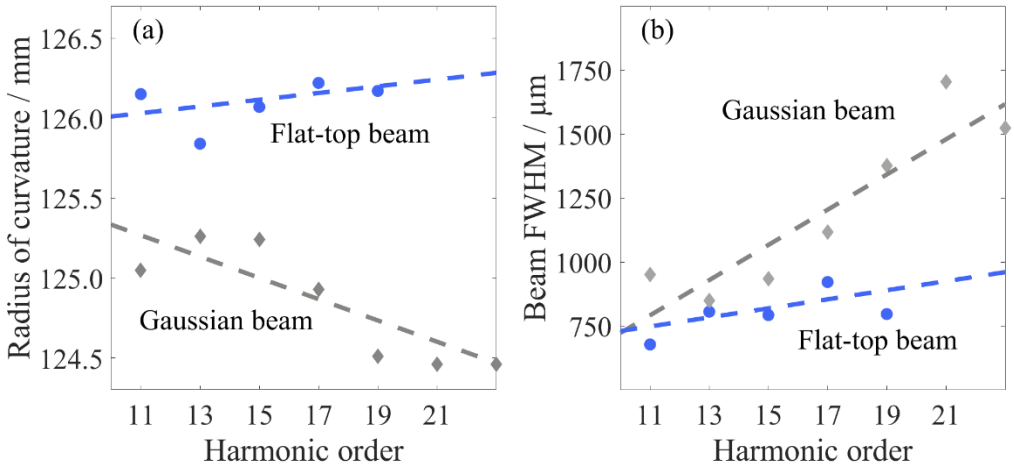

Fig. S5. (a) Radii of curvature, R_q, and (b) beam sizes (FWHM) of the harmonics generated with a Gaussian beam (diamond markers) or with a flat-top shaped beam (circle symbols). Harmonics are generated in a 1cm long gas cell.

These results provide the waist size and positions when harmonics are generated with a Gaussian driver (Fig. S6 (a) and (c)) or with a flat-top driver (Fig. S6 (b) and (d)). The on-axis harmonic intensities are represented in both cases, and we observe that the foci positions are well separated when harmonics are emitted with a Gaussian beam and less separated when generated with a flat-top beam. Fig. S6 also shows the evolution of the on-axis mean photon energy and bandwidth. As with a gas jet, we observe that the evolution is less pronounced with the flat-top beam than with the Gaussian beam.

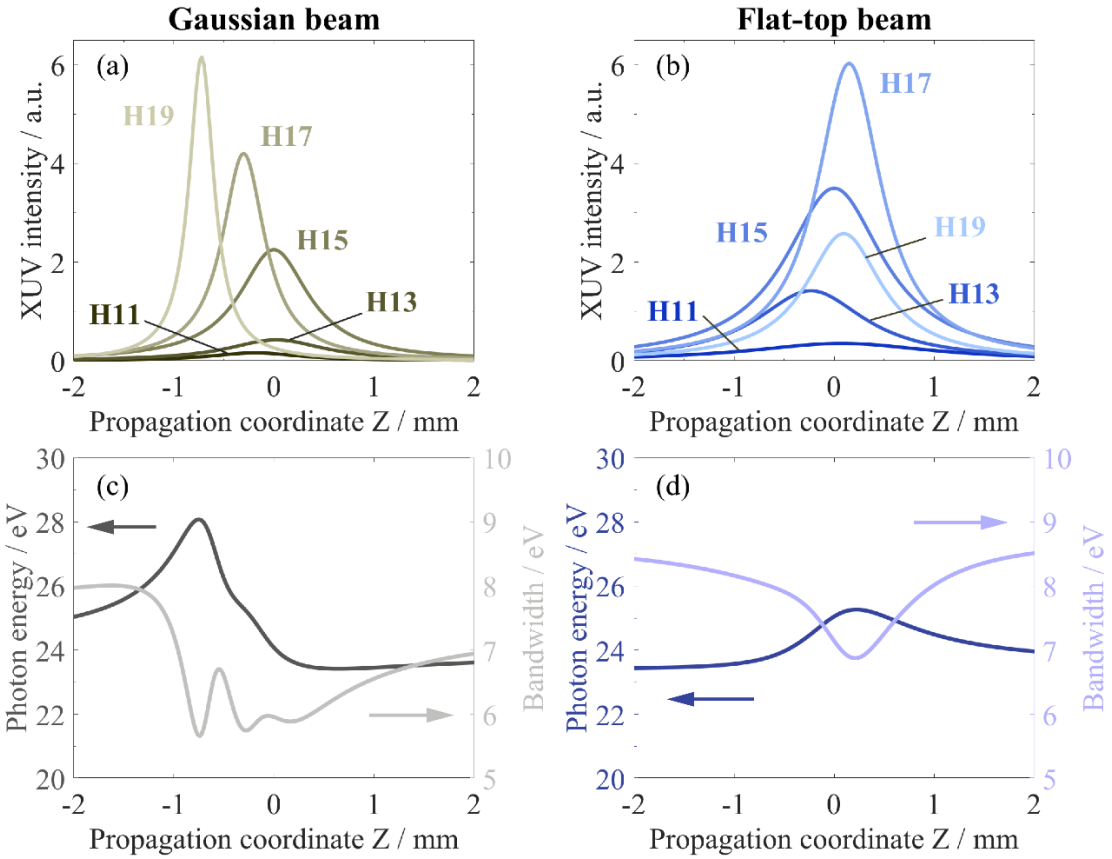

Fig. S6: Harmonic beam characteristics near XUV focus for harmonics generated with a Gaussian ((a) and (c)), respectively a flat-top shaped ((b) and (d)) fundamental beam in a 1 cm long gas cell (on-axis intensities for harmonics 11 to 19, on-axis mean photon energy and on-axis bandwidth). Z = 0 is arbitrarily set to the position of the focus of harmonic 15.

Complementary to the results obtained with a gas jet (Fig. 7), Fig. S7 contains the results obtained with a 1 cm gas cell indicating the same difference between a Gaussian fundamental beam and the flat-top shaped driver.

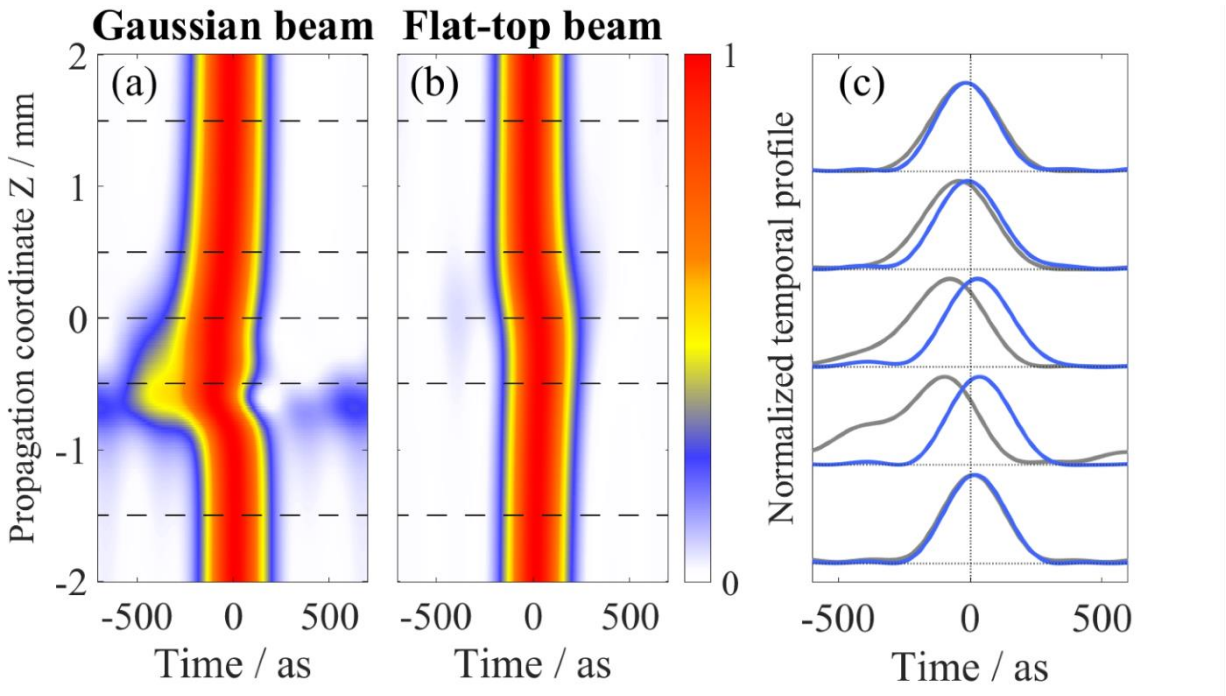

Fig. S7. Spatial evolution of the attosecond temporal profile for harmonics 11 to 19 emitted in a 1 cm gas cell with a Gaussian fundamental beam (a) or a flat-top shaped fundamental beam (b). The corresponding temporal profiles are shown in subfigure (c) (Gaussian: grey line, Flat-top: blue line) for some longitudinal positions (Z = -1.5 mm, -0.5 mm, 0 mm, 0.5 mm and + 1.5 mm; ordered from bottom to top), as indicated by the dashed line in the temporal profile

The main paper draws conclusions by considering only the harmonics H11 to H19, generated both with the flat-top and Gaussian beams. Fig. S8 and S9 show the evolution of the attosecond pulse profile with propagation considering all harmonics. We also observe an evolution of the attosecond pulse profile and timing that is more pronounced with the Gaussian beam (S8) than with the flat-top beam (S9).

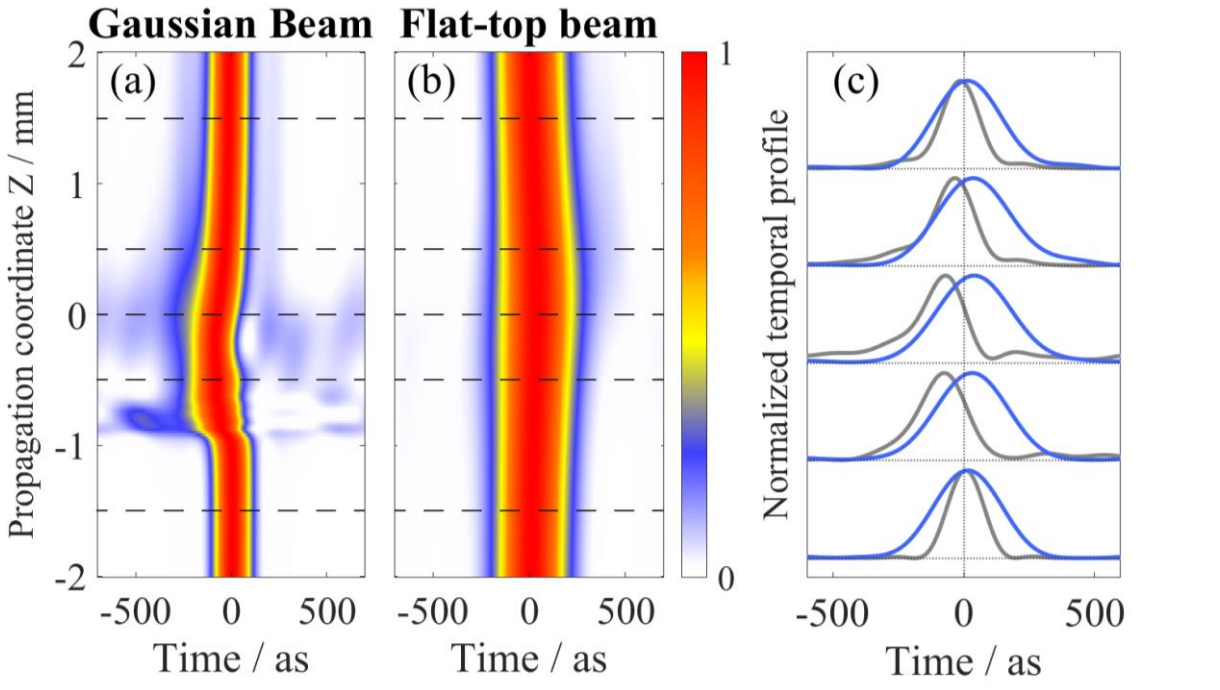

Fig. S8: Spatial evolution of the temporal profile when all harmonics are considered. Harmonics generated in a gas jet with either a Gaussian (a) or flat-top shaped (b) fundamental beam. (c): Corresponding normalized temporal pulse profile (Gaussian: grey line, Flat-top: blue line) for some longitudinal positions (Z = -1.5 mm, -0.5 mm, 0 mm, 0.5 mm and + 1.5 mm; from bottom to top), indicated as dashed lines in the temporal profile.

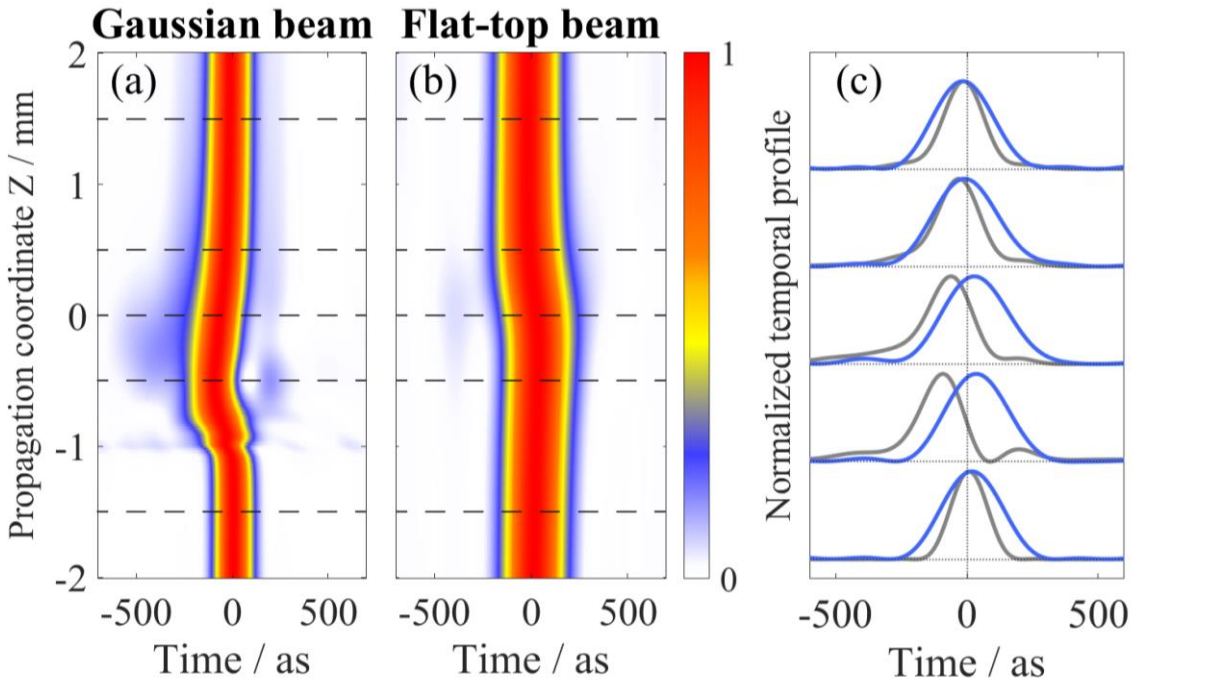

Fig. S9: Spatial evolution of the temporal profile when all harmonics are considered. Harmonics generated in a 1 cm gas cell with either a Gaussian (a) or flat-top shaped (b) fundamental beam. (c):

Normalized temporal pulse profile (Gaussian: grey line, Flat-top: blue line) for some longitudinal positions (Z = -1.5 mm, -0.5 mm, 0 mm, 0.5 mm and + 1.5 mm; from bottom to top), indicated as dashed lines in the temporal profile to the left.

Fig. S10 (a) shows the harmonic spatial profile measured on the slit plane and the Gaussian fits used in the analysis. The fits are very good for the main part of the peaks. The profile measured on the MCP (Fig. S10 (b)) is also shown with a Gaussian estimate that is not a fit, but an estimate obtained from the sword analysis that considers only measurements on the slit plane. The agreement observed between measured and estimated profiles is good. Harmonics considered in Fig. S10 are generated with a flat-top beam. Similarly, Fig. S11 exhibits harmonics emitted using a Gaussian beam. The agreement between, measurements, fits and estimates are also very good.

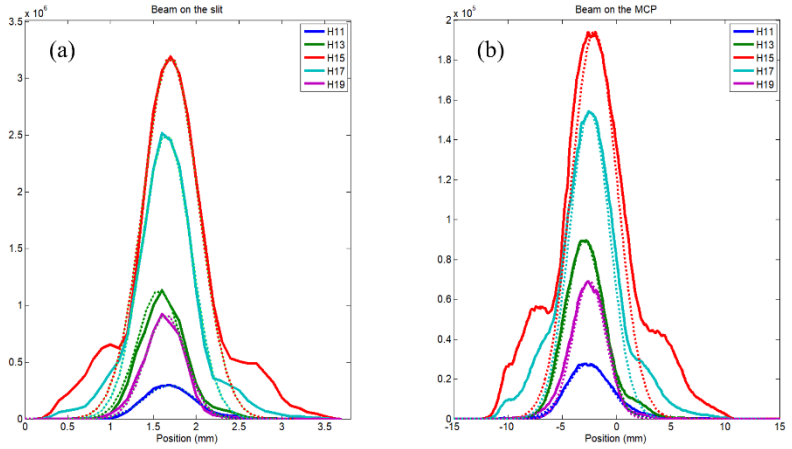

Fig. S10: XUV profiles obtained with a flat-top IR beam and HHG in a gas jet. (a) Spatial profiles measured in the slit plane and Gaussian fit (dots) used for the Gaussian analysis. (b) Spatial profiles measured on the MCP detector and Gaussian spatial profiles (dots) estimated from the sword analysis relying on measurements in the slit plane.

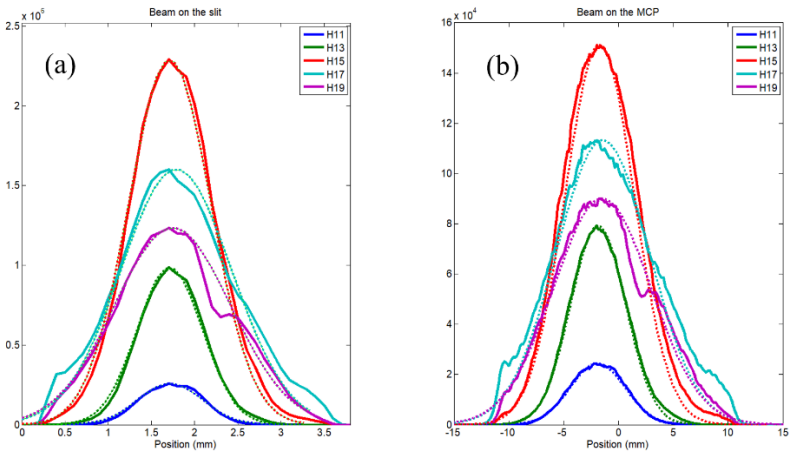

Fig. S11: XUV Spatial profiles obtained with a Gaussian fundamental beam and HHG in a gas jet. (a) Spatial profiles measured in the slit plane and Gaussian fit (dots) used for the Gaussian analysis. (b)

Spatial profiles measured on the MCP detector and Gaussian spatial profiles (dots) estimated from the sword analysis relying on measurements in the slit plane.

Advanced simulations were performed with TDSE as presented in the text. Fig. S12 shows that the focusing properties are very different for harmonics generated with a Gaussian beam (longitudinally separated foci) compared to a flat-top beam (overlapping foci). Simulations also show that temporal profiles evolve more with propagation in the Gaussian case than in the flat-top case.

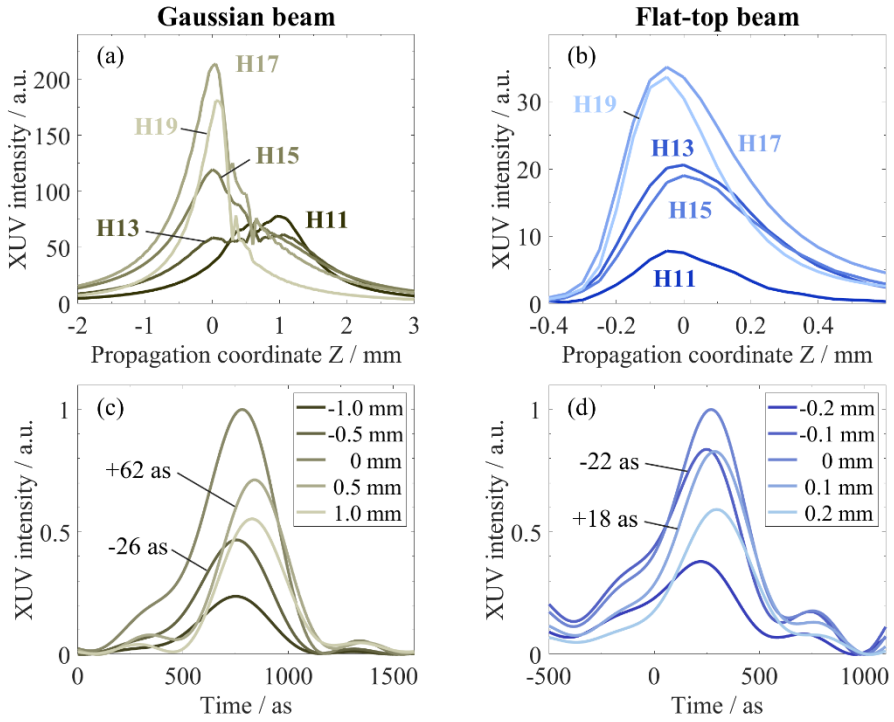

Fig. S12: XUV-intensity along the propagation axis for harmonic 11 to 19 generated by a IR Gaussian beam (a), and a flat-top respectively (b). Evolution of the attosecond temporal profile for truncated Gaussian (c) and flat-top beams (d) for a peak intensity of I = 2x10^{14} W/cm^2. The numbers in (c) and (d) (+62, -26, -22 and +18 as) indicates the shift of the pulse relative to the Z = 0 mm reference.

For the Gaussian case, the observed increase of the XUV beam size with IR intensity (see Fig. 3. (a)) is not reproduced by the simulations within the approach described above which neglects propagation in the generating medium. To reproduce this evolution, we mimic propagation in a simple way and include an additional dephasing, due to the medium ionization, and the impact of the plasma refractive index. The plasma index evolves radially, affecting the IR beam wavefront. This transverse phase, multiplied by the harmonic order, is transferred to the harmonic beam. This plasma defocusing of the IR leads to corresponding defocusing of the harmonics that is more pronounced with increasing harmonic order. With a gas density that corresponds to an absorption length close to the medium length, we find that plasma defocusing has a strong impact in the Gaussian case (strong intensity gradient and high intensity) but a low impact in the flat-top case (low gradient and low intensity). The simulations consider the plasma defocusing quantitatively reproduce the experimentally observed increase of the XUV beam size with IR intensity and harmonic order. The plasma defocusing also reduces the foci shift by essentially suppressing the XUV light present on axis for Z > 5mm (Fig. S11). The defocusing reduces the evolution of the

attosecond pulse duration during propagation but leads to a significant displacement of the center of the atto pulse that can shift by more than 100 as over one mm of longitudinal propagation (Fig. S13).

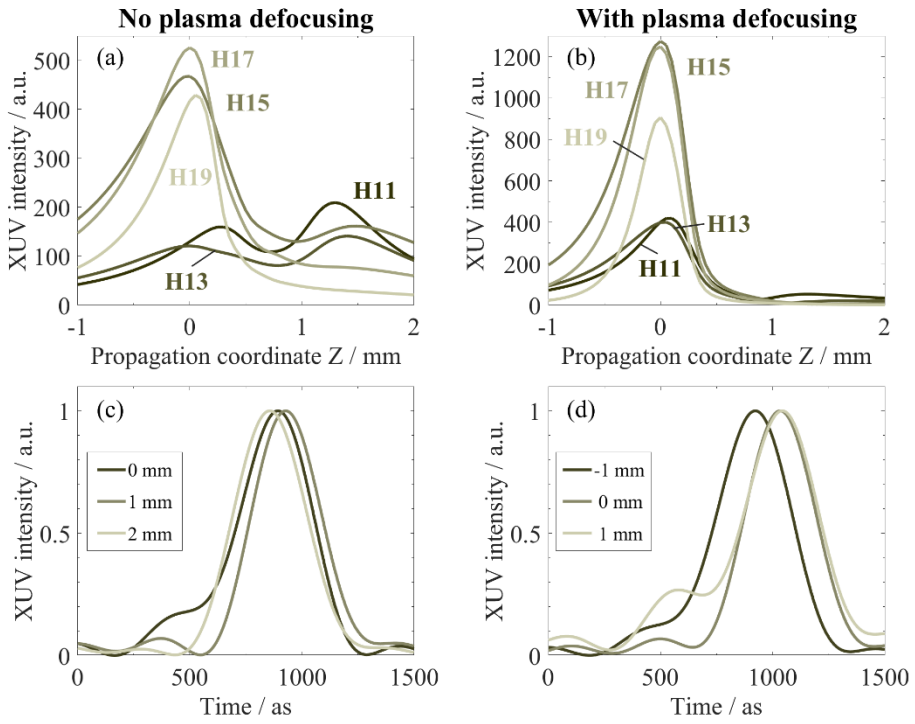

Fig. S13: On axis harmonics signal for harmonics generated with a truncated Gaussian beam at high intensity (a) without and (b) with the plasma defocusing. Corresponding on axis attosecond profile without (c) and with (d) plasma defocusing at an IR peak intensity of $3.5x10^{14}$ W/cm^2.

For comparison, we simulate the XUV focusing with and without plasma defocusing. The results are shown in Fig. S13. We observe that the plasma defocusing of the IR tends to clean the XUV focusing by essentially suppressing the XUV components that were present at large Z without defocusing. Nevertheless, with the plasma defocusing also, the temporal profile of the attosecond pulses emitted by the Gaussian beam evolves with propagation and the temporal profile near focus differs significantly from the asymptotic pulse profile. There again, the pulse duration changes with propagation and a temporal shift is present as observed experimentally.